

CHAPTER IV RESULTS AND DISCUSSION

4.1 Characterization of Organically-Clay Filler

4.1.1 FTIR

The chemical characteristics of both the organic and inorganic materials can be studied by IR spectra analysis. Figure 4.1 (a) shows FTIR spectra of sodium-montmorillonite (Na-MMT) compared with (b) bis (hydrogenated tallow) dimethyl ammonium chloride (OH) and (c) bis (hydrogenated tallow) dimethyl ammonium chloride-montmorillonite (OH-MMT).

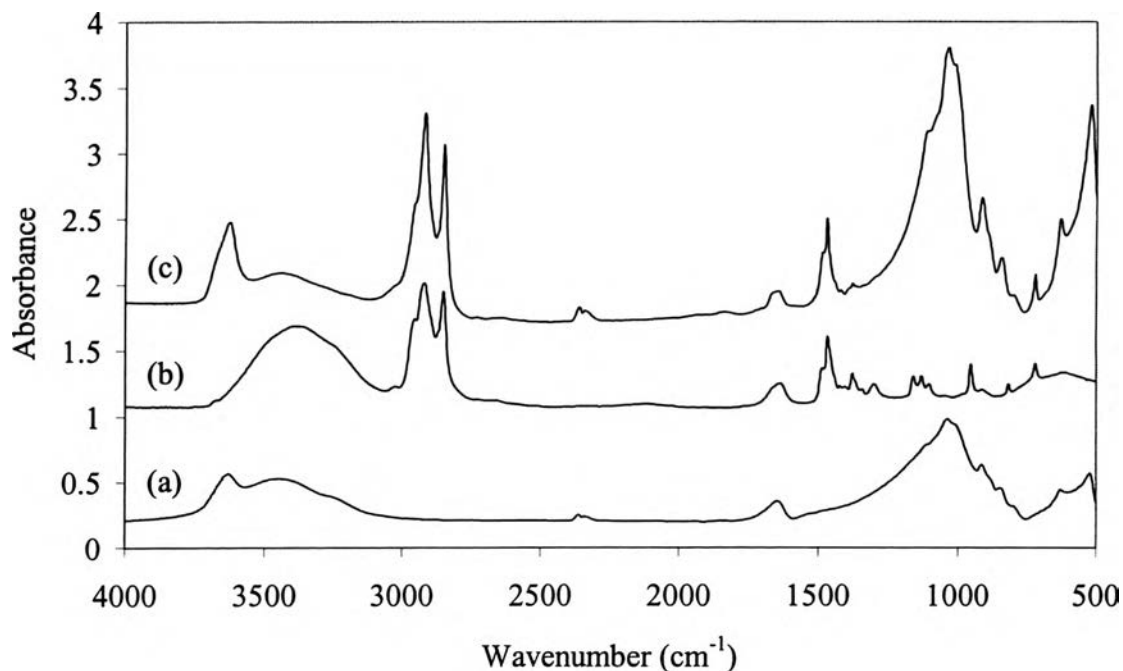


Figure 4.1 FTIR spectra of (a) Na-MMT, (b) OH, and (c) OH-MMT.

FTIR spectrum of OH-MMT shows the specific absorption characteristics of both inorganic and organic components with respect to aluminosilicate layers and the alkylammonium molecules. As seen in the IR spectra

of Figure 4.1, all assignments of Na-MMT, OH , and OH-MMT are summerized in Tables 4.1-4.3, respectively.

Table 4.1 FTIR absorption bands assignment of sodium-montmorillonite

Frequencies (cm ⁻¹)	Assignments
3620	-OH stretching
3440	-OH stretching (dimers)
1040	Si-O stretching
720	N-H out of plane bending
520	Al-O stretching
466	Si-O bending

Table 4.2 FTIR absorption bands assignment of OH

Frequencies (cm ⁻¹)	Assignments
3366	-OH stretching
2950	C-H stretching of methyl group
2850	C-H stretching of methylene group
1430	C-H stretching of ammonium ion

Table 4.3 FTIR absorption bands assignment of OH-MMT

Frequencies (cm ⁻¹)	Assignments
3620 3440	-OH stretching
2950	C-H stretching of methyl group
2850	C-H stretching of methylene group
1430	C-H stretching of ammonium ion
1040	Si-O stretching
720	N-H out of plane bending
520	Al-O stretching
466	Si-O bending

4.1.2 WAXD

The strong supported evidence for the incorporation of modifying agent into montmorillonite structure was obtained from WAXD. The X-ray diffraction spectra of Na-MMT and organically modified montmorillonite or OH-MMT in the region from $2\theta = 2^\circ$ to $2\theta = 10^\circ$ are demonstrated in Figure 4.2 (a) and (b). From this figure, each curve has d_{001} spacing at $2\theta = 7.20^\circ$ and 2.32° , respectively. Peak position of OH-MMT is transitioned to lower 2θ angles relative to that of Na-MMT. This is indicated that the distances between silicate layers are expanded significantly due to the incorporation of modifying agent into the MMT structure. The interlayer distances are calculated from peak position of basal spacing. Therefore, the interlayer spacing of Na-MMT found in this work is 12.17 Å. After treatment via ion-exchange reaction, the interlayer spacing of OH-MMT is measured to be 37.08 Å.

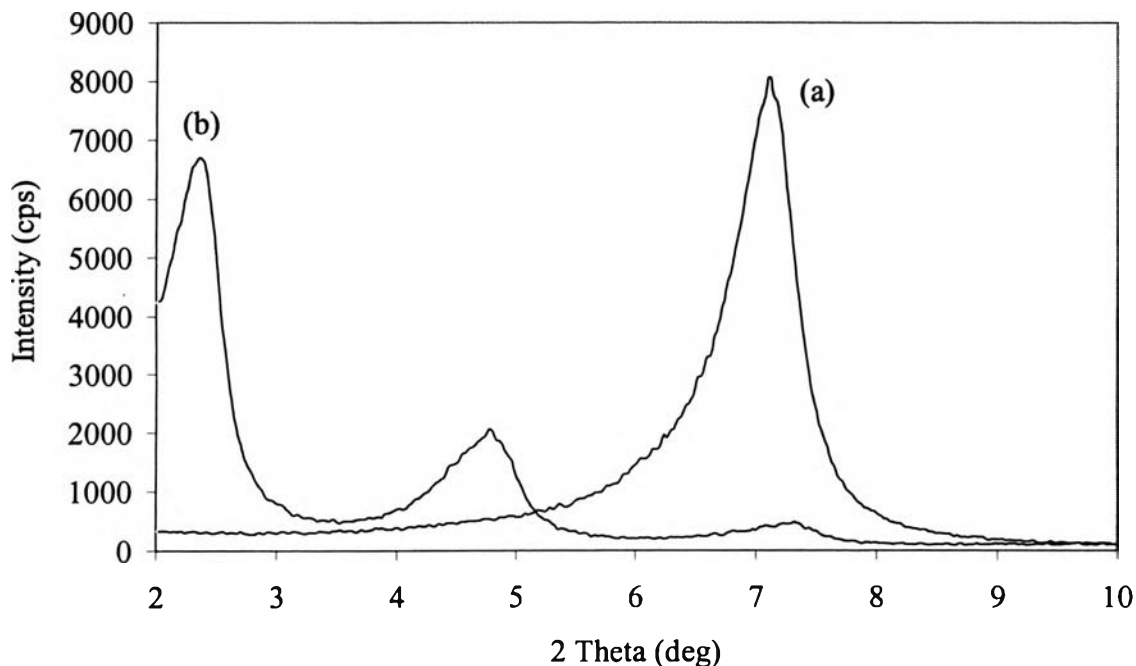


Figure 4.2 WAXD patterns of (a) Na-MMT and (b) OH-MMT.

4.1.3 TGA

As well as WAXD, thermogravimetric analysis is applied to confirm the incorporation of modifying agent into montmorillonite structure. TGA thermograms for Na-MMT, OH, and OH-MMT are given in Figure 4.3. The decomposition temperature (T_d) is obtained from the derivative TGA thermogram. As evident from Figure 4.3, T_d of modifying agent, OH, is found approximately 180°C while T_d of Na-MMT is around 655°C. It is observed that improvement in thermal stability of modifying agent resided between silicate layers could be substantiated by the thermogram of OH-MMT which shows T_d at 328 °C. The reason for the improvement in T_d of modifying agent is resulted from the ionic force between alkylammonium ion and negative charge of montmorillonite.

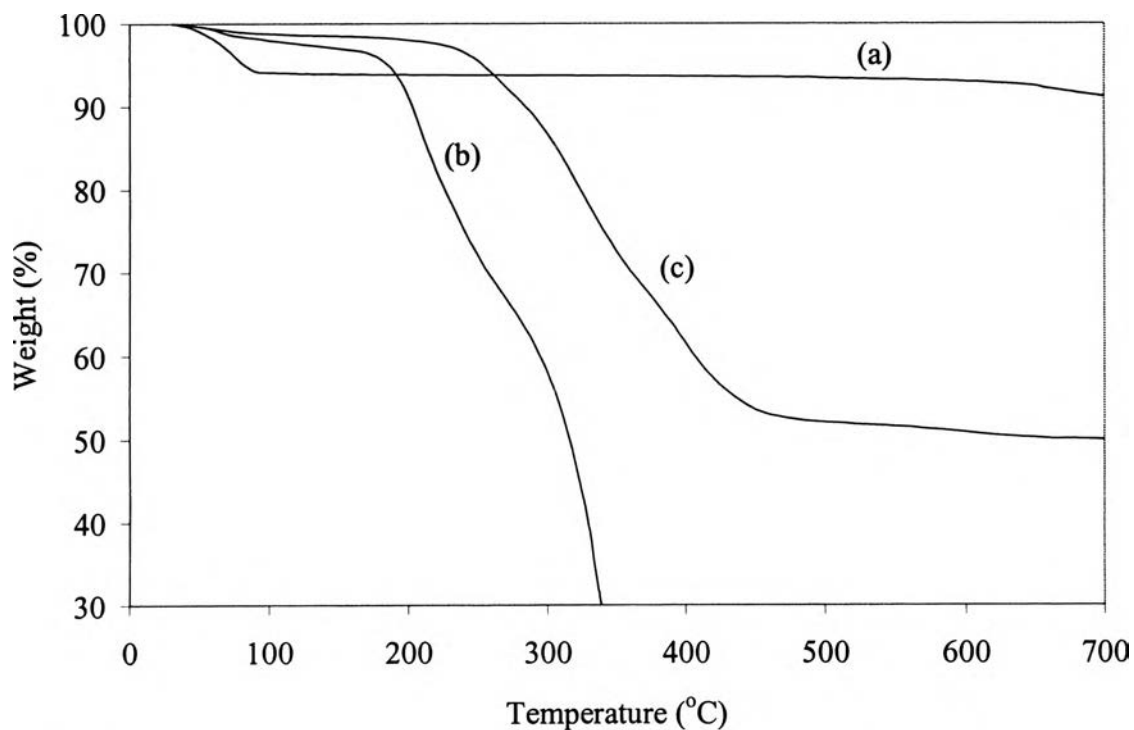


Figure 4.3 TGA thermograms of (a) Na-MMT, (b) OH, and (c) OH-MMT.

4.1.4 AAS

The purity of the organophilic-montmorillonite was determined by measuring a recovery percentage of sodium ions in an acidic solution. The percentage of ions exchange from Na-MMT in the process of preparation of organically-clay was determined by the air acetylene flame AAS. The percentage conversion of organophilic-clay can be calculated by the following expression.

$$\text{Na}^+ \text{- exchanged percentage} = \frac{(\text{Amount of Na}^+ \text{ in solution obtained from AAS}) \times 100}{(\text{Weight of montmorillonite} \times 119e^{-5})}$$

Consequently, the percentage of sodium ions exchange was equal to 96.16%. Preparation of standard solution for calibration curve is demonstrated in Appendix A.

4.2 Characterization of Poly (*p*-phenylene vinylene) (PPV)

4.2.1 FTIR

The polymerization reactions of the sulfonium salt monomers were carried out in methanol solution under nitrogen at the lowest practical temperature, 0°C, in order to minimize the subsequent elimination reaction on the polymer, which forms units of PPV. After that, an equivalent amount of sodium hydroxide was added. The initial reaction is a proton abstracting by the base on the benzylic position of the monomer do form the sulfur ylid (Burn *et al.*, 1992) as shown in Figure 4.4.

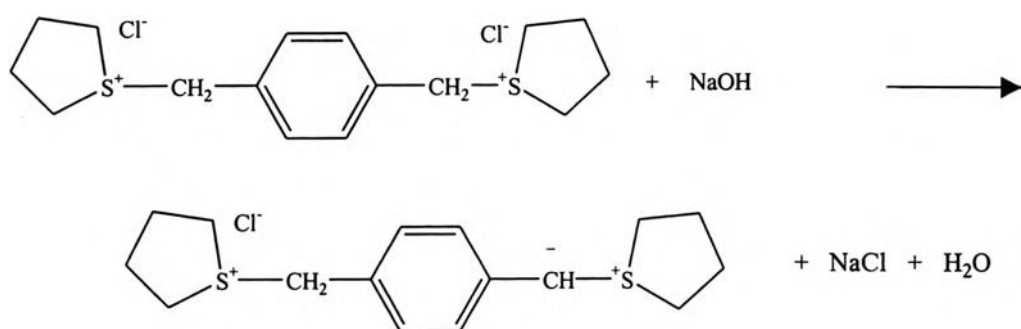


Figure 4.4 Formation reaction.

The ylid most likely undergoes a 1,6 elimination reaction to form the *p*-xylene sulfonium chloride which is the true monomer of the polymerization reaction as shown in Figure 4.5. The polymerization was carried out by addition reaction in Figure 4.6.

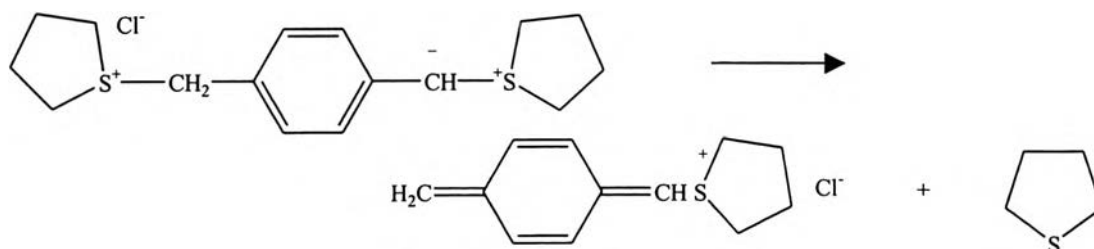


Figure 4.5 1,6-Elimination reaction.

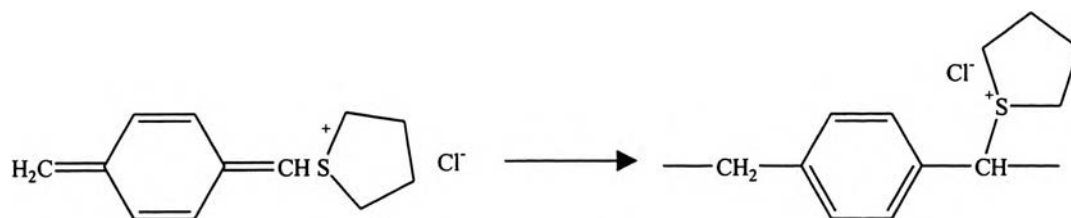


Figure 4.6 Addition reaction.

The polymerization reactions were terminated by the addition of aqueous solutions of HCl until pH = 7 was reached and the resulting aqueous solutions of the precursor polymer were dialyzed to remove the low molecular weight byproducts and unreacted monomers. Undoubtedly, a low molecular weight fraction of the polymers was also lost because of the permeability properties of the membrane used. The cut off molecular weight of dialysis membrane is 6000. The IR spectrum and appearance of precursor polymer film is shown in Figure 4.7 and 4.8, respectively.

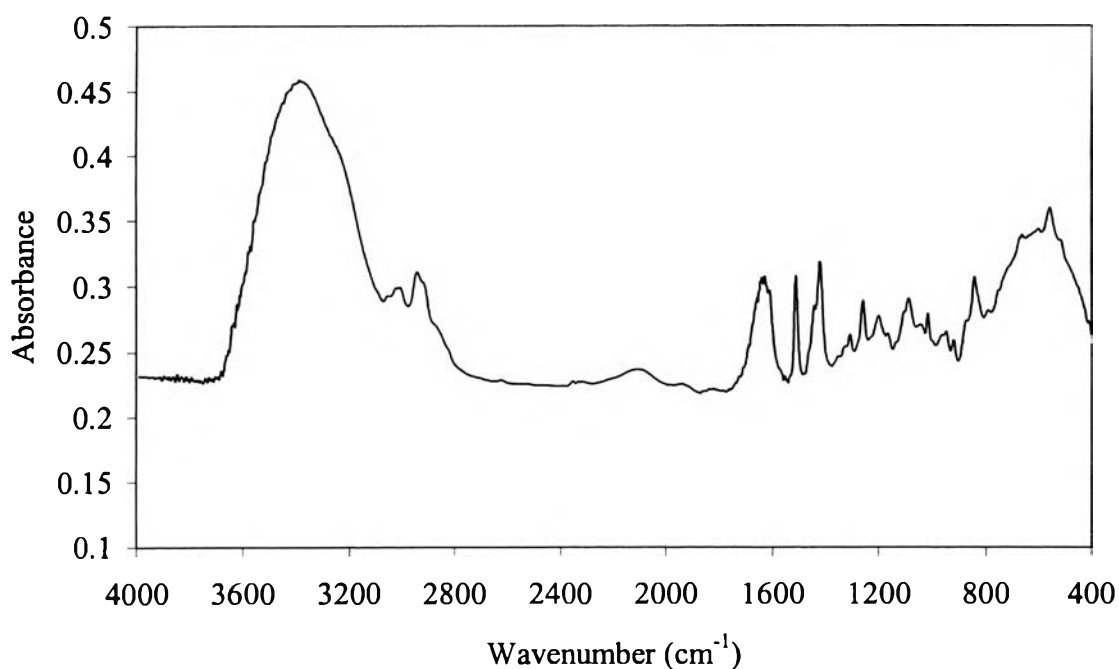


Figure 4.7 FTIR spectrum of precursor polymer.



Figure 4.8 Appearance of precursor polymer.

After that, conversion to PPV was done by heating to 200°C for 16 hours in vacuum oven to remove all of the water, organic sulfides and HCl. The resultant homogeneous, dense films were brownish yellow in color, see Figure 4.9.

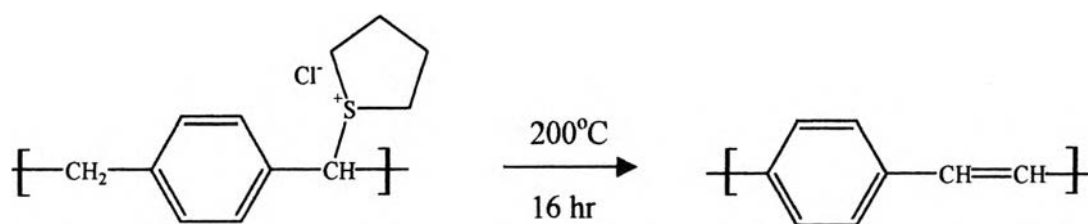


Figure 4.9 Thermal elimination to PPV.

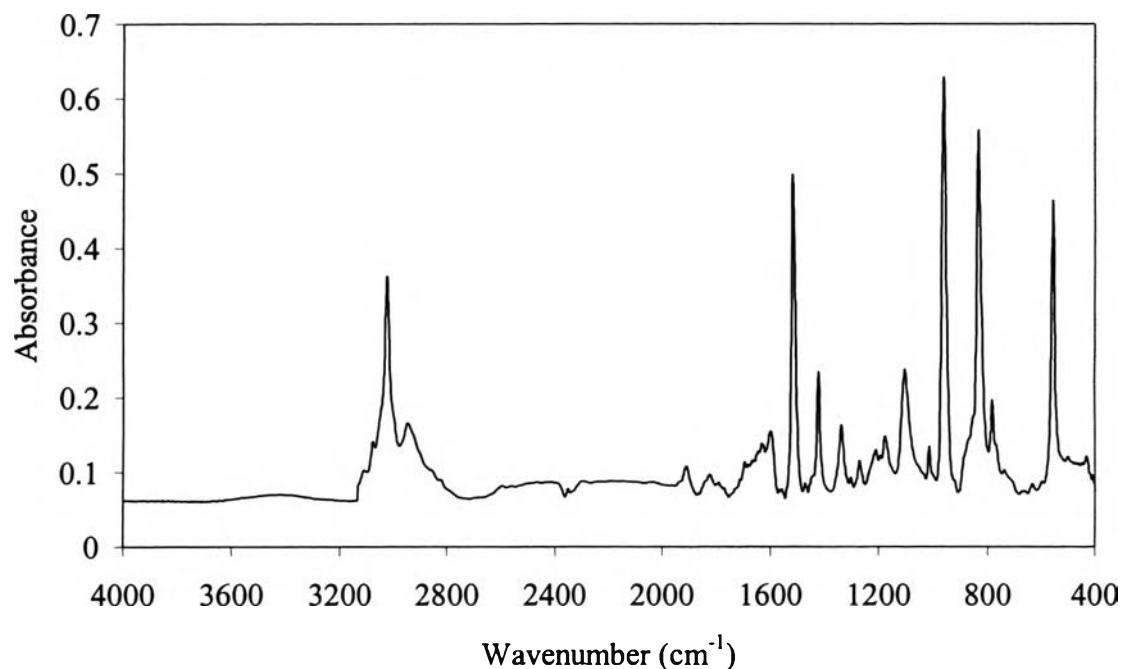


Figure 4.10 FTIR spectrum of PPV.

IR spectroscopy has been proved to be a useful technique to study the molecular and electronic structure of PPV. In Figure 4.10, nearly all the large peaks are assigned to the *p*-phenylene ring which is present in both precursor polymer and fully converted PPV except the broad peak at 3375 cm⁻¹ due to the solvent OH-stretch band. Peaks at 555, 837, 964, 1015 cm⁻¹ are assigned to *p*-phenylene out of plane ring bend, phenylene ring CH out of plane bend, trans-vinylene CH out of plane bend and in plane phenylene bend, respectively. The band at 3024 cm⁻¹ is assigned to a trans-vinylene CH stretching mode.

Frequencies of the IR-active modes in PPV are concluded in Table 4.4. In addition, appearance of PPV is shown in Figure 4.11.

Table 4.4 FTIR absorption bands assignment of poly(*p*-phenylenevinylene)

Frequencies (cm ⁻¹)	Assignments
3105	Aromatic C-H stretching
3024	Trans-vinylene C-H stretching
2950	C-H stretching from remnant saturated aliphatic groups
1594 1519 1421 1336	C-C ring stretching
1267 1176 1102	C-H in-plane bending
964	Trans-vinylene C-H out of plane bending
837	Phenylene ring C-H out of plane bending
555	Phenylene out of plane ring bending

(a)



(b)

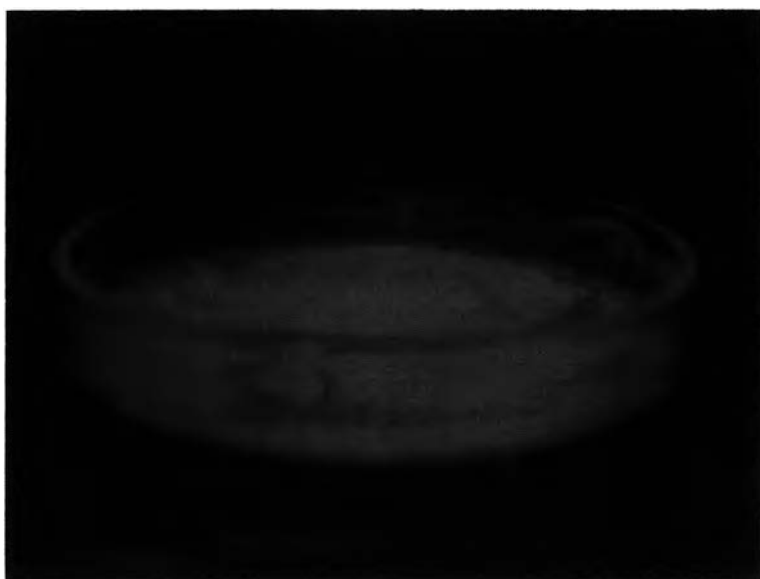


Figure 4.11 Appearance of PPV (a) without UV radiation, (b) with UV radiation.

4.2.2 UV-Vis and Photoluminescence

The absorption spectra and photoluminescence emission spectra of PPV are shown in Figure 4.12 and 4.13, respectively. UV-Vis spectrum is determined in order to illustrate the optical properties that are important for the conducting polymer. The optical properties of the conducting polymer are generally considered in terms of absorption wavelength, which can be converted to photon energy in electron volt units (eV) by using Einstein's equation as

$$E = h\nu = \frac{hc}{\lambda} \quad (4.1)$$

Where E is photon energy (J), h is Plank's constant which is equal to 6.62×10^{-34} J-sec, ν is the frequency (Hz or s^{-1}), c is the light velocity in vacuum, which is equal to 3×10^8 m/sec and λ is the wavelength (nm or m) of the light.

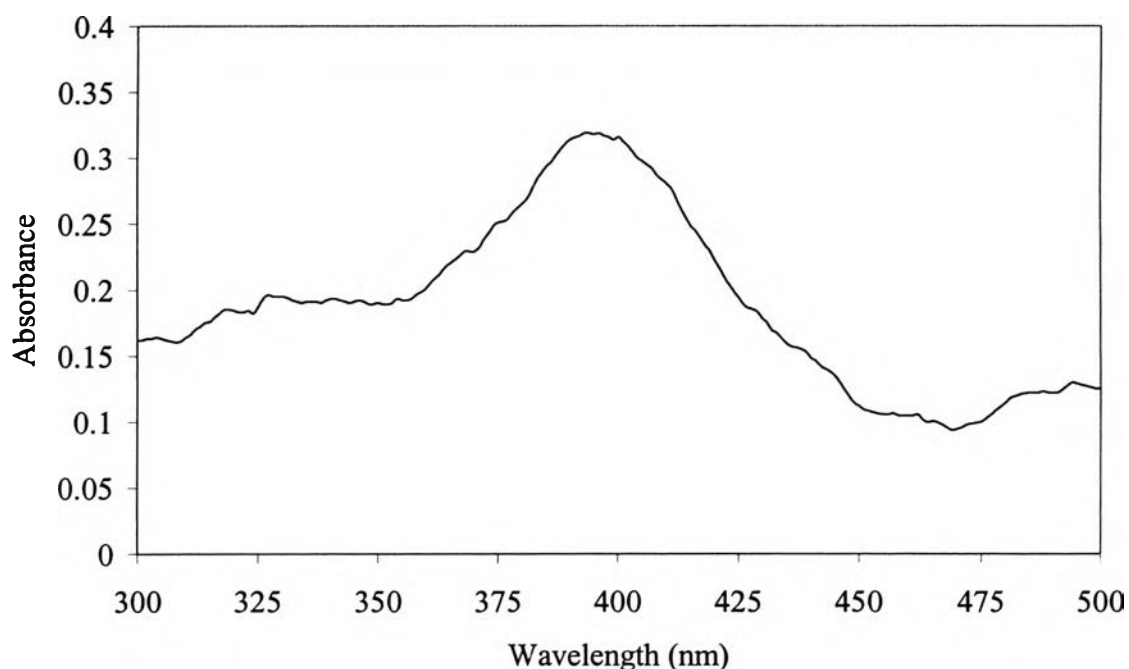


Figure 4.12 UV-Vis spectrum of PPV.

From the absorption spectra of PPV, the maximum absorption peak is about 480 nm (2.58 eV). When the material is excited at an energy which falls into one of its absorption band, electrons are excited from the ground state to the vibrational levels of higher electronic states. As excited electrons return to a lower energetic state, excess energy can be emitted as a photon, resulting in luminescence. This light is recognized by its usually longer wavelength, compared with the exciting radiation. The emission maxima at 550 nm (2.25 eV) and 520 nm (2.38 eV) of PPV are in the yellow-green region of the visible spectrum as shown Figure 4.13.

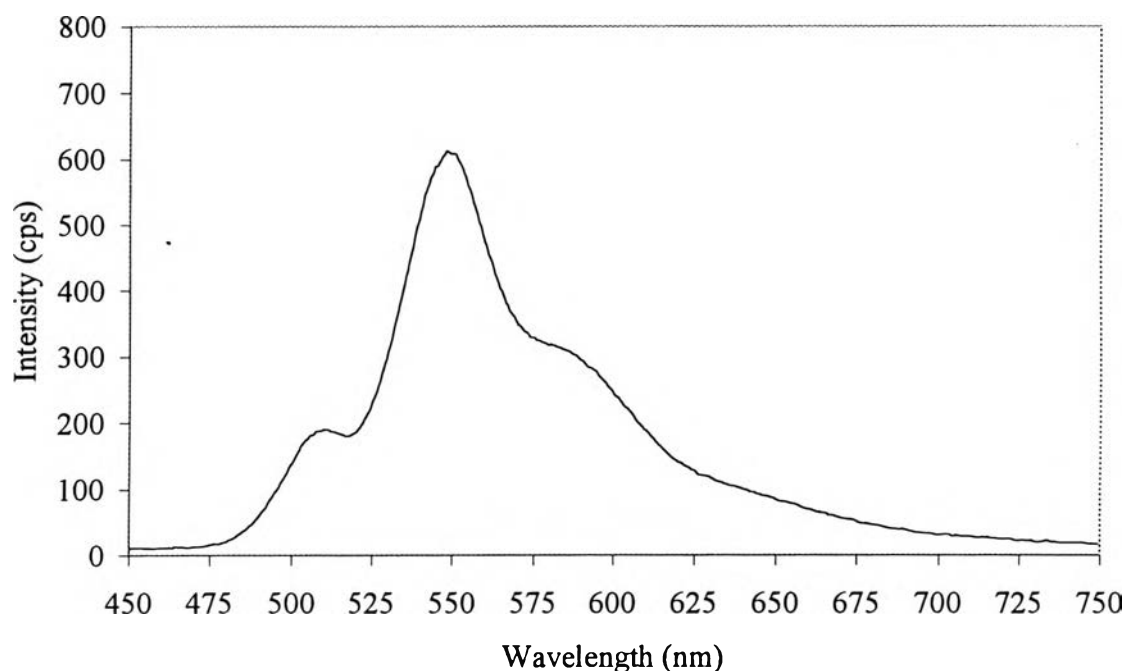


Figure 4.13 Photoluminescence spectrum of PPV.

4.3 Characterization of Protein Extracted from the Scales of Seabass

4.3.1 FTIR

Photoluminescence extraction from the scales of seabass was desired to determine the protein content of organic substances by the Kjeldahl method illustrated in Appendix B. The chemical structure of protein was characterized by FTIR spectroscopy as shown in Figure 4.14. Although the precise sequence of amino acids of the seabass scales was unknown at this time, some major absorbance bands were seen. For protein, there are the assignments from the peptide bond.

First, the absorption band at 3300 and 1655 cm^{-1} is due to NH stretching and C=O stretching. The band near 1543, 1480, and 1241 cm^{-1} are all assigned to CN stretching and NH bending. Next, the band at 765 cm^{-1} is assigned to the OCN bending mode of peptide bond. In addition, the absorption bands at 602 and 562 cm^{-1} correspond to the out-of-plane C=O bending. The other bands may be resulted from the functional group of amino acids. Table 4.5 suggests some amino acids contributing the potentially photoluminescence property and the appearance of protein extracted from the scales of seabass is demonstrated in Figure 4.15.

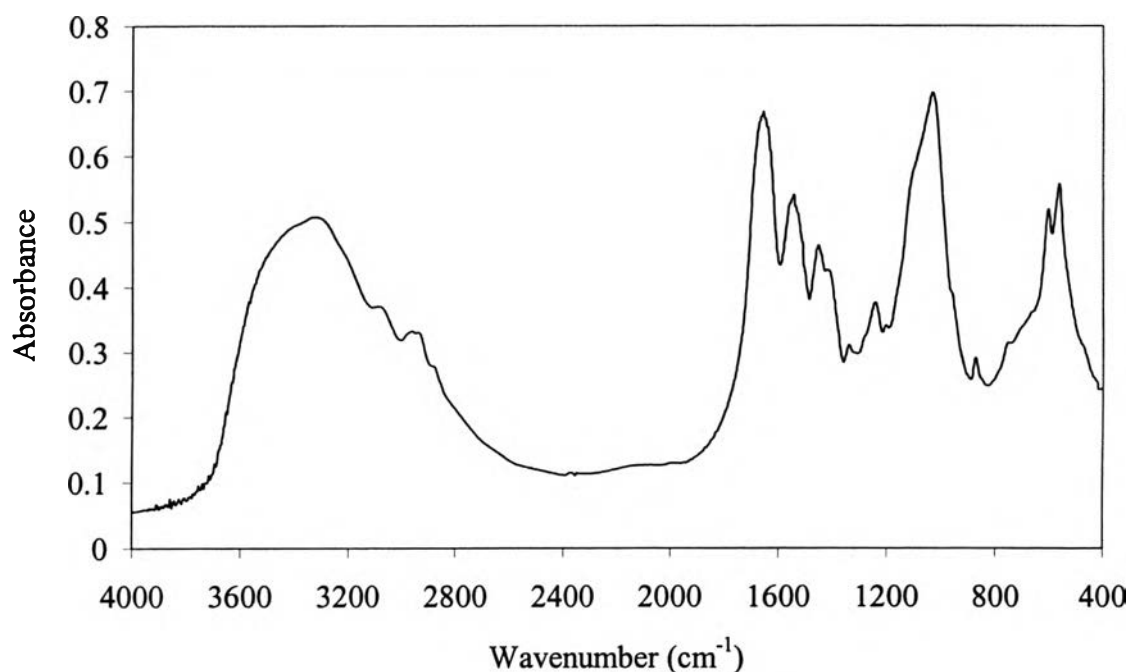
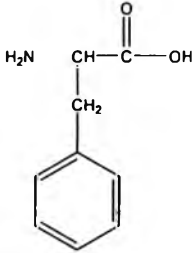
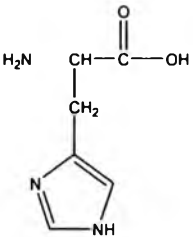
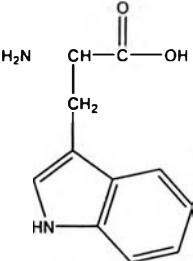
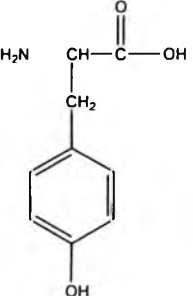


Figure 4.14 FTIR spectrum of protein extracted from the scales of seabass.

Table 4.5 The suggested amino acids containing conjugated bonds and aromatic rings that can function as chromophores

No.	Amino acid	Chemical structure
1	Phenylalanine (Phe)	 <chem>N[C@@H](Cc1ccccc1)C(=O)O</chem>
2	Histidine (His)	 <chem>N[C@@H](Cc1c[nH]cn1)C(=O)O</chem>
3	Tryptophan (Trp)	 <chem>N[C@@H](Cc1c[nH]c2ccccc12)C(=O)O</chem>
4	Tyrosine (Tyr)	 <chem>N[C@@H](Cc1ccc(O)cc1)C(=O)O</chem>

(a)



(b)

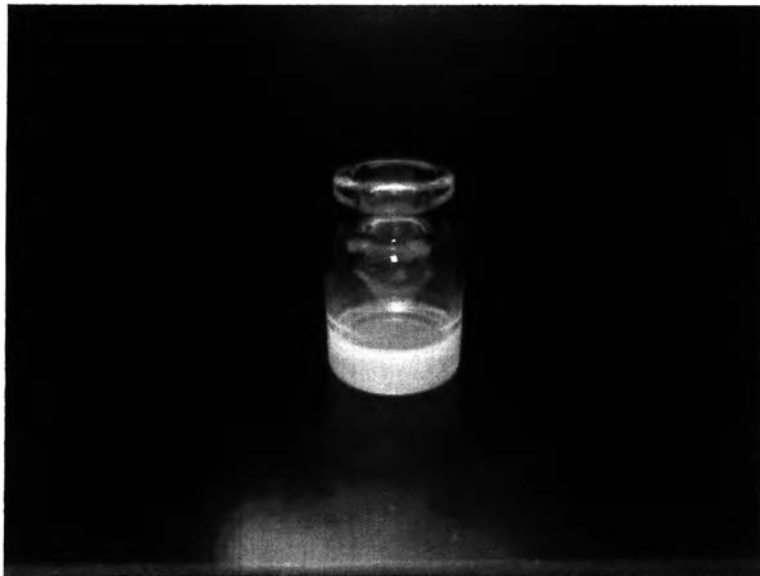


Figure 4.15 Appearance of protein extracted from the scales of seabass
(a) without UV radiation, (b) with UV radiation.

4.3.2 UV-Vis and Photoluminescence

UV-Vis absorption and photoluminescence emission results are shown in Figures 4.16 and 4.17, respectively. The absorption demonstrated the highest peak at 390 nm.



Figure 4.16 UV-Vis spectrum of protein extracted from the scales of seabass.

Photoluminescence occurs when electrons return to the electronic ground state from an excited state and loss their energy as a photon. Therefore, protein extracted from the scales of seabass was excited by a monochromatic light at 410 nm. The photoluminescence exhibited the blue light with a maximum peak at 483 nm.

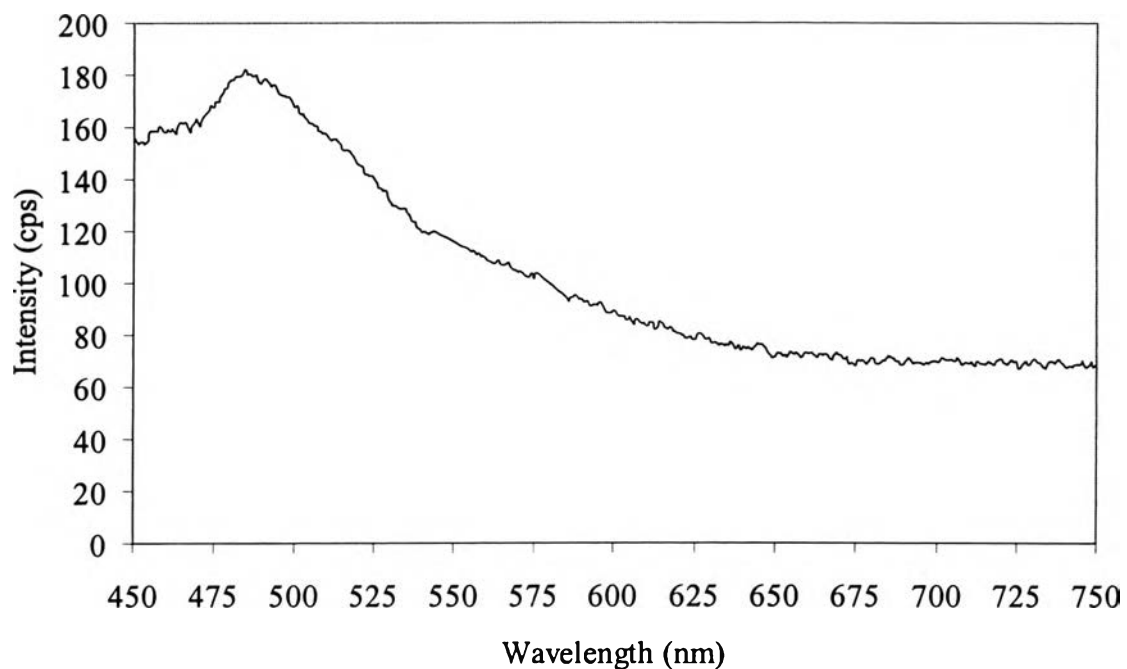


Figure 4.17 Photoluminescence spectrum of protein.

4.4 Characterization of Polymer-Clay Nanocomposites

4.4.1 FTIR

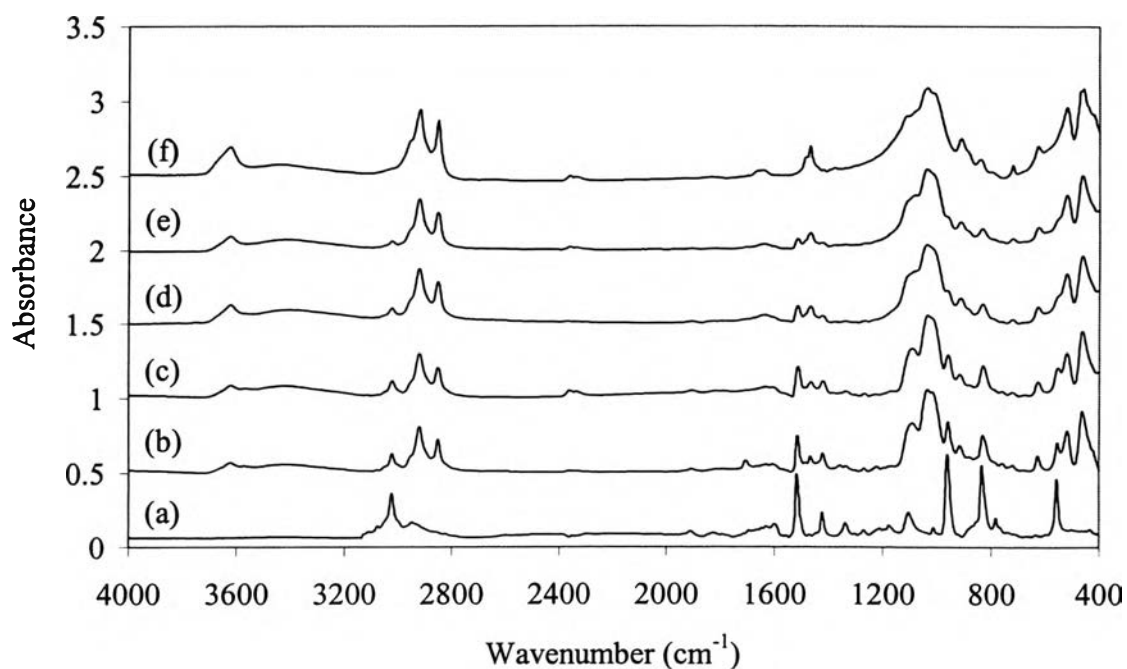


Figure 4.18 FTIR spectra of (a) PPV, PPV/OH-MMT (b) 30 wt %, (c) 40 wt %, (d) 50 wt %, (e) 60 wt %, and (f) MMT-OH.

FTIR spectroscopy can be used to characterize the chemical characteristics of the polymer-clay nanocomposites. Figures 4.18 and 4.19 illustrate FTIR spectra of polymer with various clay contents in the nanocomposites and the spectrum of organophilic montmorillonite.

FTIR spectra of PPV-clay nanocomposites as shown in Figure 4.18 exhibit the presence of characteristic absorption due to both the organic and the specific filler component. The bands at 3620, 2950, 2850, 1430, 1040, 720, 520, and 460 cm^{-1} can be associated with OH stretching, C-H stretching of methyl group, C-H stretching of methylene group, C-H stretching of ammonium ion, Si-O stretching, N-H out of plane bending, Al-O stretching, and Si-O bending, respectively. Clearly seen from this figure, absorptions of these peaks increase with increasing clay loading. Not only the modified montmorillonite nanocomposites of PPV show both the pristine PPV and clay filler but also FTIR spectra of protein extracted from the scales of seabass and its nanocomposites exhibit typical peaks of both polymer and organophilic clay combined together according to their contents as shown in Figure 4.19.

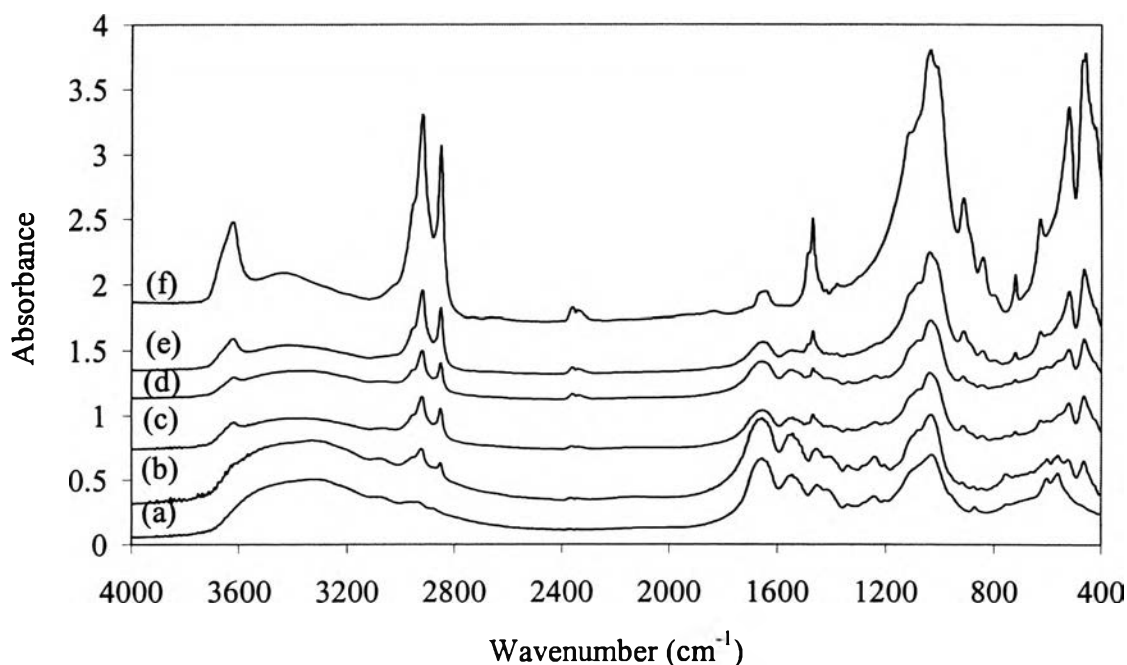


Figure 4.19 FTIR spectra of (a) protein extracted from seabass, protein/OH-MMT (b) 30 wt %, (c) 40 wt %, (d) 50 wt %, (e) 60 wt %, and (f) MMT-OH.

4.4.2 WAXD

WAXD results of various contents of modified montmorillonite are shown in Table 4.6 and their spectra demonstrate in Figure 4.20. These data explain the relationship between the peak shift to lower 2θ angle correlates with the higher polymer loading.

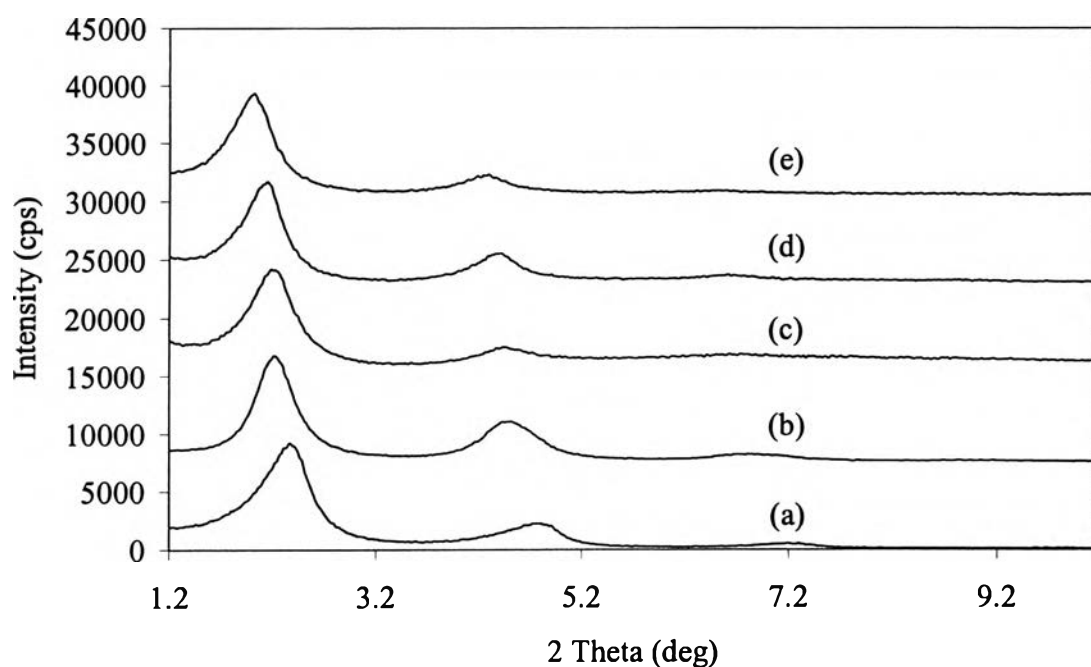


Figure 4.20 WAXD patterns of (a) MMT-OH, PPV/OH-MMT (b) 30 wt %, (c) 40 wt %, (d) 50 wt %, and (e) 60 wt %.

Table 4.6 Basal spacing of PPV-clay nanocomposites

PPV loading (wt %)	Clay loading (wt %)	Basal Spacing (Å)
0	100	37.40
40	60	39.76
50	50	40.12
60	40	41.63
70	30	43.70

This revealed the presence of silicate layers existed in an intercalated form which is a particular type of the clay nanocomposites as described by Pinnavaia *et al.* (1996). In addition, The same trend of WAXD spectra was observed for both PPV and protein. Protein-clay nanocomposites prepared by solution techniques with clay loading of 30, 40, 50, and 60 wt % can also be classified as an intercalated nanocomposite due to the X-ray diffraction patterns in the low 2θ range found in Figure 4.21 and Table 4.7, respectively.

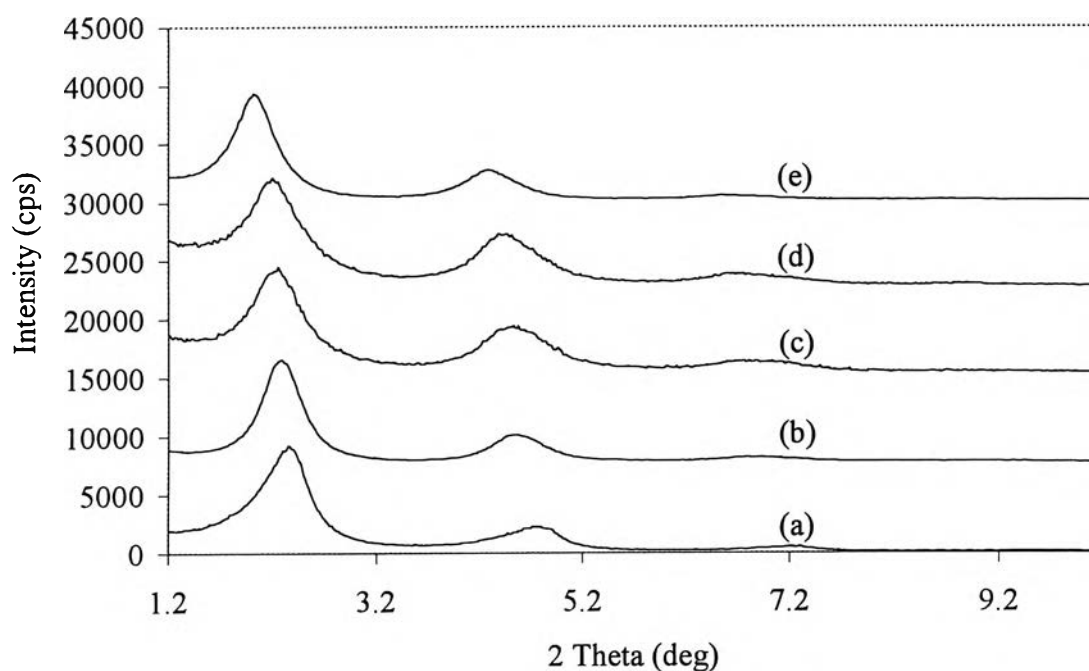


Figure 4.21 WAXD patterns of (a) MMT-OH, protein/OH-MMT (b) 30 wt %, (c) 40 wt %, (d) 50 wt %, and (e) 60 wt %.

Table 4.7 Basal spacing of protein-clay nanocomposites

Protein loading (wt %)	Clay loading (wt %)	Basal Spacing (Å)
0	100	37.40
40	60	38.72
50	50	39.41
60	40	40.12
70	30	43.27

4.4.3 TEM

Not only structural characterization of polymer layered silicate nanocomposites has centered around X-ray diffraction, but the observation has also revealed by Transmission Electron Microscopy (TEM). Figure 4.22 is a TEM bright-field image of an organically modified layered silicate 40 wt % intercalated with PPV. Individual crystallites of the silicate are visible as regions of alternating narrow, dark, and light bands within the particle. The structural characterization of protein extracted from scales of seabass-clay nanocomposites obtained by TEM.

From WAXD result, protein nanocomposites formed from OH-MMT with various percentage of clay are all intercalated clay nanocomposites. Representative examples of polymer/layered silicate nanocomposites morphologies are shown in Figure 4.23 and 4.24. In general, an extended polymer chain is intercalated between the host layers resulting in a well order multilayer with alternating polymer/inorganic host layers and a repeat distance of a few nanometers.

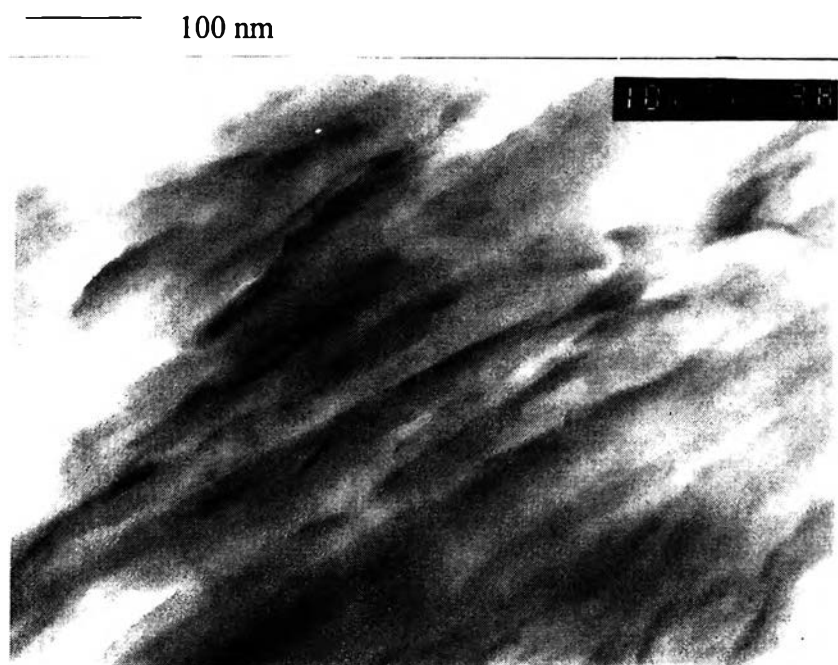


Figure 4.22 Transmission electron micrograph of PPV-clay nanocomposites 40 wt % (magnification = 100000X).

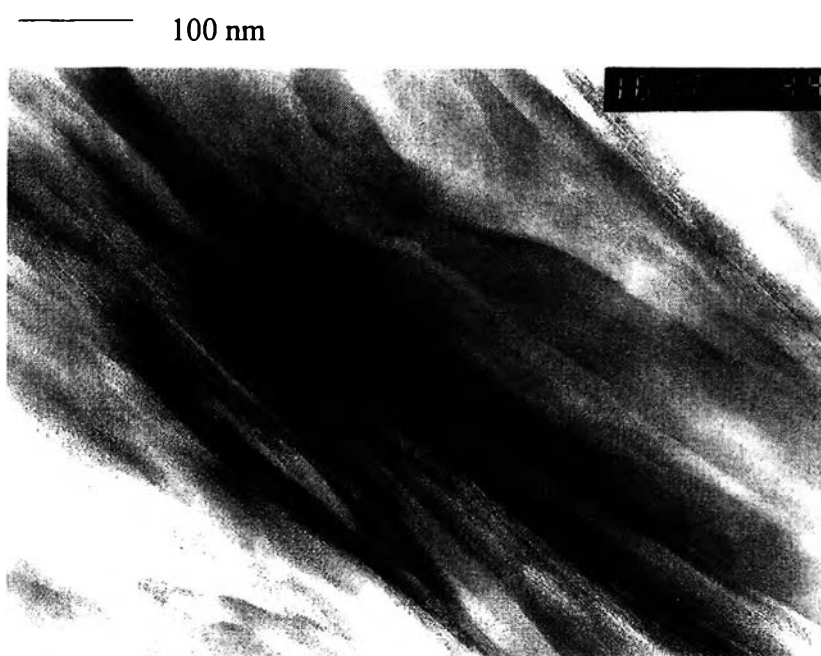


Figure 4.23 Transmission electron micrograph of protein-clay nanocomposites 30 wt % (magnification = 100000X).

4.4.4 TGA

Thermogravimetric analysis was used for study the effect of polymer/layered silicate nanocomposites. The decomposition temperatures (T_d) of both PPV-clay nanocomposites and protein-clay nanocomposites are shown in Tables 4.8 and 4.9, respectively. From the result, the decomposition temperatures of polymer/layered silicate nanocomposites shifted to lower temperature with increasing clay content. It is meant that thermal stability of PPV and protein extracted from the scales of seabass was not improved by nanocomposites with OH-MMT.

Table 4.8 The first and second decomposition temperatures of PPV/OH-MMT

Clay loading (wt %)	Decomposition temperature (°C)	
	Td#1	Td#2
30	291.12	416.36
40	283.67	400.73
50	276.98	400.05
60	273.31	396.38

Table 4.9 The first and second decomposition temperatures of protein/OH-MMT

Clay loading (wt %)	Decomposition temperature (°C)	
	Td#1	Td#2
30	53.79	330.71
40	52.87	329.80
50	49.79	332.49
60	47.78	330.47

4.5 Properties Measurement

4.5.1 Color Tunability Measurement

Figure 4.24 demonstrates the PL spectra of PPV and PPV-clay nanocomposites. The PPV emitted green light with an emission maximum around

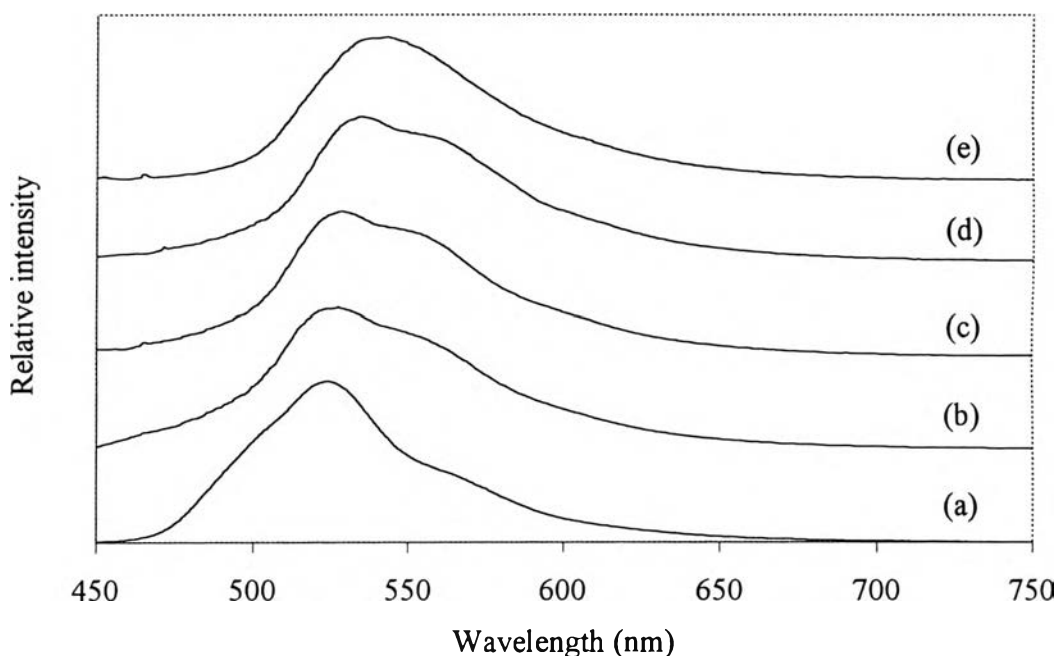


Figure 4.24 Photoluminescence spectra of (a) PPV, (b) PPV-clay 30 wt %, (c) 40 wt %, (d) 50 wt %, and (e) 60 wt %.

524 nm. The introduction of clay nanoparticles into PPV led to a significant red shift (longer conjugated length) in PL spectra, obviously seen by the shift at the beginning of the emission wavelength. The PPV-clay 30 and 40 wt % nanocomposites emitted a maximum peak at 527.5 nm with a shoulder at 550.5 nm and a maximum peak at 529.5 with a shoulder at 553 nm, respectively. Next, Yellow-green light emission maximum was observed from PPV-clay 50 wt % nanocomposites with an emission maximum at 536 nm with a shoulder at 562 nm. In addition, the PPV-clay 60 wt % nanocomposites emitted a maximum peak at 542.5 nm without shoulder.

The PL spectra of protein and its nanocomposites were similar to PPV and its nanocomposites as shown in Figure 4.25. The PL emissions with increasing intercalation level were shifted to longer wavelength. The emission spectra of the pristine protein showed emission band with the maximum peak at 484.5 nm. The

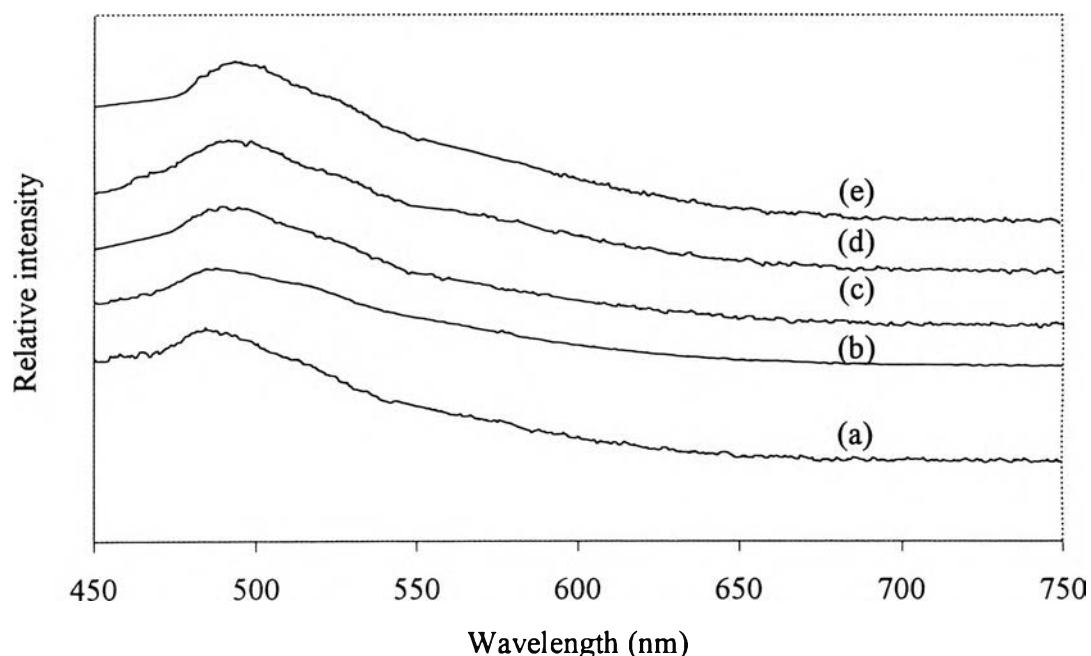


Figure 4.25 Photoluminescence spectra of (a) protein, (b) protein-clay 30 % wt, (c) 40 wt %, (d) 50 wt %, and (e) 60 wt %.

protein-clay nanocomposites at 30, 40, 50, and 60% wt emitted blue-green light with a maximum peak at 488, 490, 491.5, and 493.5 nm, respectively. This features are contributed to an intercalation-induced conformation transition from a “compact coil” to “extended coil”. When the polymer chains are intercalated in the 2-dimensional confined geometry, the effective conjugation length should increase due to the chain planarization. (Lee *et al.*, 2001). The increasing of π -conjugation chain length in the intercalated polymer shows a red shift of luminescence peak wavelength.

It is clearly seen that the light emission spectrum could be tuned by controlling the ratios of polymer to clay.

4.5.2 Water Absorption

Thermogravimetric analysis was used for study on water absorption of polymer and polymer-clay nanocomposites (Lilayuthalert, 1998). Weight loss of PPV-clay nanocomposites and protein-clay nanocomposites are illustrated in Figures 4.26 and 4.27, respectively. Generally, the water absorption of PPV and protein are very high because the water molecules can easily diffuse to form H-bonding along that polymer chains. The figures show that polymer it self is associated with a relatively higher weight loss, which corresponds to the removal of water.

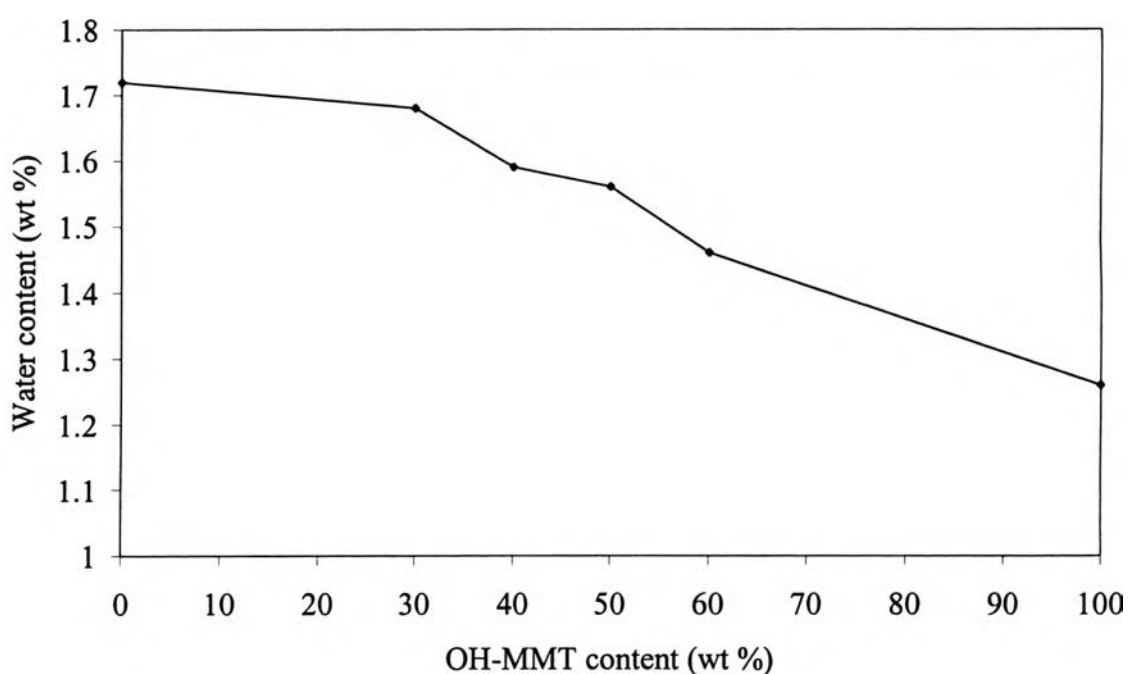


Figure 4.26 Effect of organophilic-clay on water absorption of PPV.

The reduction of diffusing water molecules is due to the stacking layer of polymer-clay nanocomposites that can act as a barrier to water diffusion into polymer. It was first reported by the Toyota researchers (Kojima *et al.*, 1993) that polyamide 6-clay hybrid had a rate of water absorption reduced by 40% as compared with the pristine polymer.

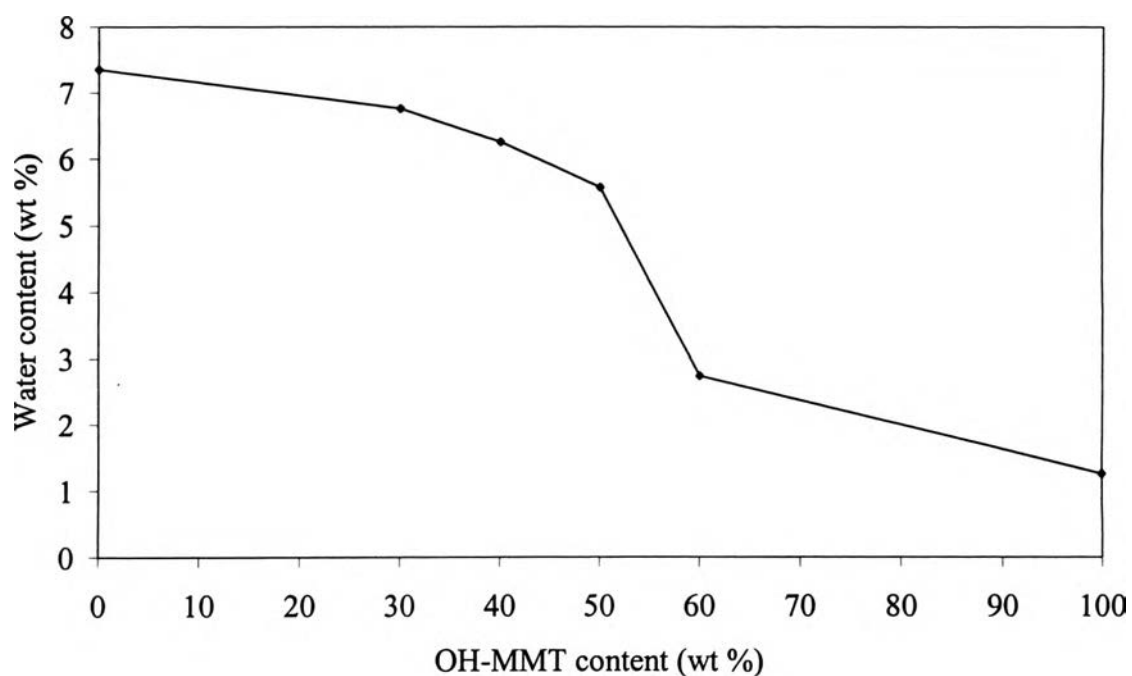


Figure 4.27 Effect of organophilic-clay on water absorption of protein extracted from the scales of seabass.

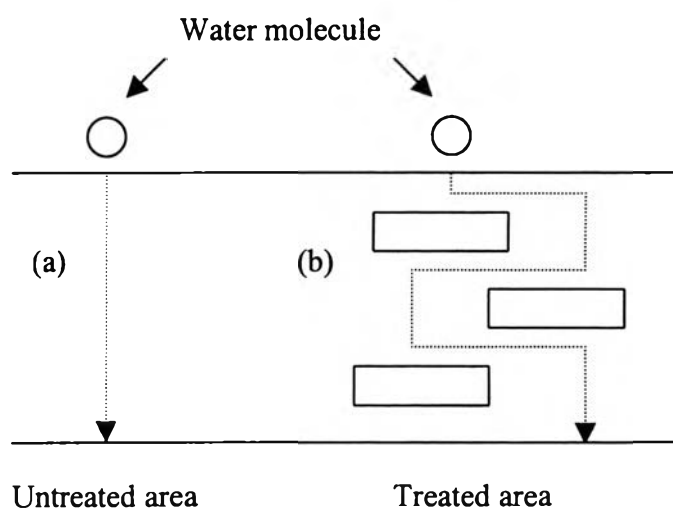


Figure 4.28 A model describing the diffusion of water molecule through polymer.

Later, Messersmith *et al.* (1995) observed a dramatic decrease of water permeability with poly (ϵ -caprolactone) layered silicate nanocomposite, up to 80 % with only 5 vol % of clay. The impressive decrease of permeability was

attributed to the clay layers which should increase the tortuosity of the path for gas and water as they diffuse into the nanocomposites (Yano *et al.*, 1993). A conceptual model describing the diffusing of gas through the polymer-clay hybrid is shown in Figure 4.28.

4.5.3 Environmental Stability

As no polymer is capable of withstanding prolonged exposure to solar radiation, stabilization of polymers is extremely important. A great deal of light induced damage to polymers is due to photo-oxidation reaction. This suggests that reactions involving oxygen and moisture are important reasons of light-emitting devices degradation. The lifetime of light-emitting polymer is compromised if they are operated in an oxygen atmosphere. Yan *et al.* (1994) have shown that the intensity of PPV emission is greatly reduced if luminescence experiments are carried out in an oxygen atmosphere rather than a nitrogen atmosphere. Then, polymer should have a low level of gas permeability to avoid any characteristic change of light-emitting devices.

The stabilization of polymer was improved by combination with organophilic-clay, which acted as photostabilizer, against severe UV-radiation. This study used polymer/layer silicate nanocomposites materials to improve the stability against oxygen and moisture. Figure 4.29 and 4.30 show the change of photoluminescence intensity at maximum peak as the function of time of PPV-clay nanocomposites and protein-clay nanocomposites, respectively while exciting with the strong monochromatic 410 nm light from a laser diode in air. The relative intensity can be calculated by using the equation as follow:

$$\text{Relative intensity} = \frac{\text{Intensity at the radiation time}}{\text{Intensity at the beginning of radiation}} \quad (4.2)$$

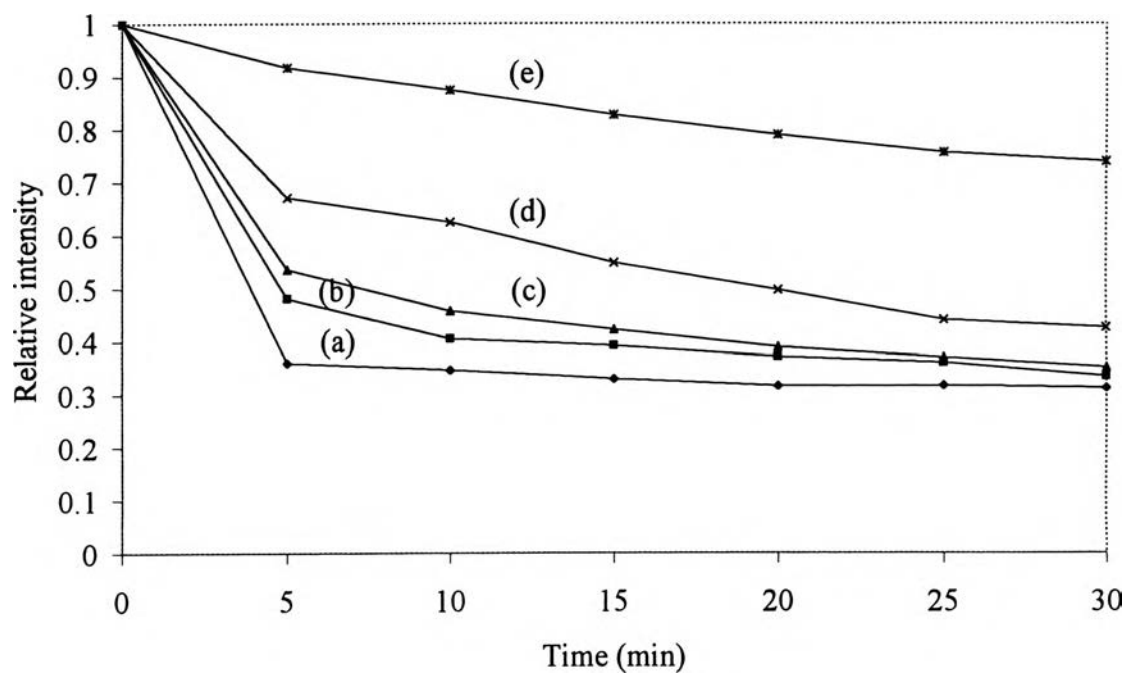


Figure 4.29 The irradiation time dependence of photoluminescence intensity of (a) PPV, PPV/OH-MMT (b) 30 wt %, (c) 40 wt %, (d) 50 wt %, and (e) 60 wt %.

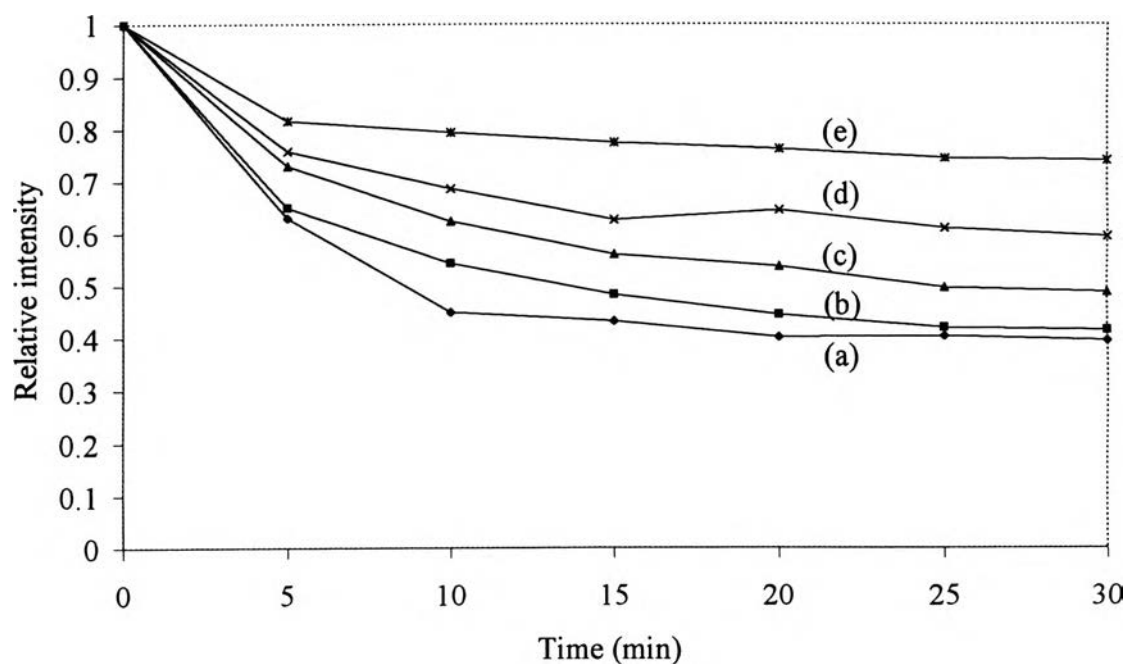


Figure 4.30 The irradiation time dependence of photoluminescence intensity of (a) protein, protein/OH-MMT (b) 30 wt %, (c) 40 wt %, (d) 50 wt %, and (e) 60 wt %.

The photoluminescence intensity of all conditions was reduced rapidly at the beginning of radiation. After that, the degradation process decreased slowly with time. The photo-oxidation of polymer-clay nanocomposites caused by the reduction of the reactive sites with oxygen is significantly inhibited (Lee *et al.*, 2002). The photoluminescence decay of each film showed different changes. It is remarkable that both pure PPV and protein thin films show the fastest decay during the same period compared with their clay nanocomposites.

Furthermore, the dependence of clay content on photoluminescence intensity was also investigated. The result showed that the higher content of clay, the slower decay of photoluminescence intensity. The confinement of exciton formation was originated from the fact that the layered silicate can effectively block the oxygen penetration into the thin film. It is concluded that the lifetime of light-emitting devices is improved by polymer-clay nanocomposites.

4.5.4 Current-Voltage Characteristics Measurement

When an organic light-emitting device is driven, singlet and triplet excitons as well as radical anions, cations (polarons), di-anions, and di-cations (bipolarons), are created. Clearly, this fact must be considered for the long-time performance of light-emitting polymers. I-V characteristics of Al/PPV-clay nanocomposites/ITO and Al/protein-clay nanocomposites/ITO sandwiched devices are shown in Figure 4.31 and 4.32, respectively.

In these light-emitting devices, Al was used as the electron-injecting electrode, and ITO was as the hole-injecting electrode. On application of an electrical voltage onto a LED device, electrons from the low work-function cathode are injected into the LUMO of the polymer-clay nanocomposites layer, leading to the formation of negatively charged polarons, whereas holes from the high work-function anode are injected into the HOMO, producing positively charged polarons. These negatively and positively charged polarons migrate under the influence of the applied electric field and combine in the band gap of polymer/layered silicate nanocomposites, resulting in the formation of the same singlet exciton as produced by the photoexcitation (Dai, 1999).

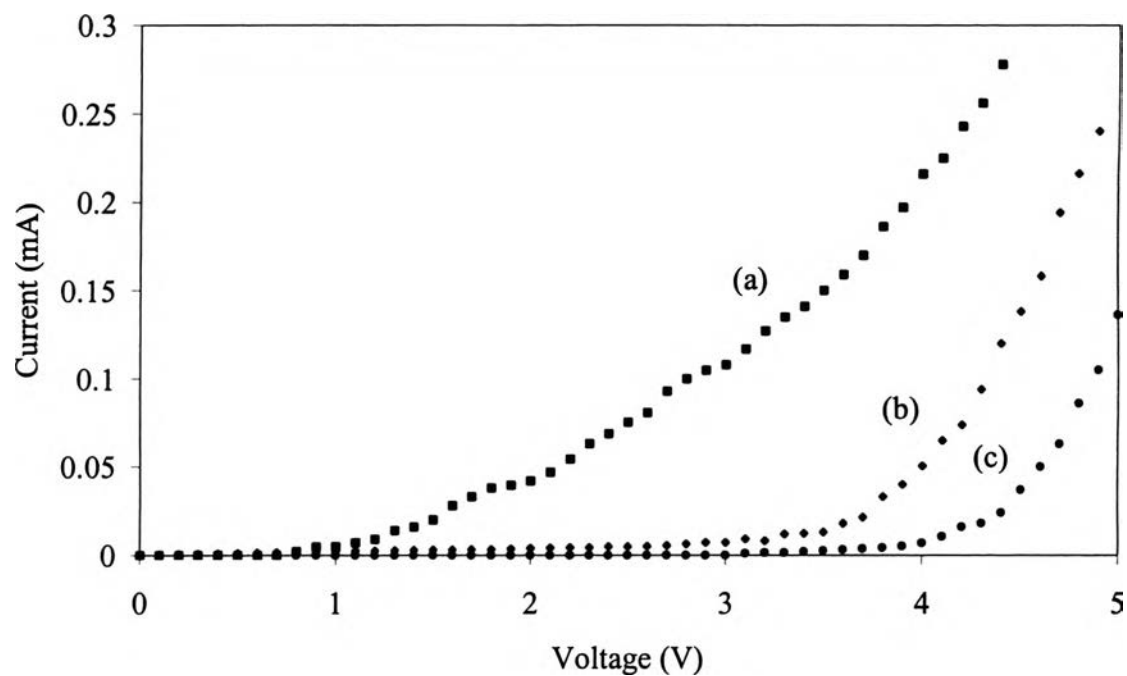


Figure 4.31 Relationship between current and voltage of LEDs based on (a) PPV, (b) PPV/OH-MMT 30 wt %, and (c) PPV/OH-MMT 60 wt %.

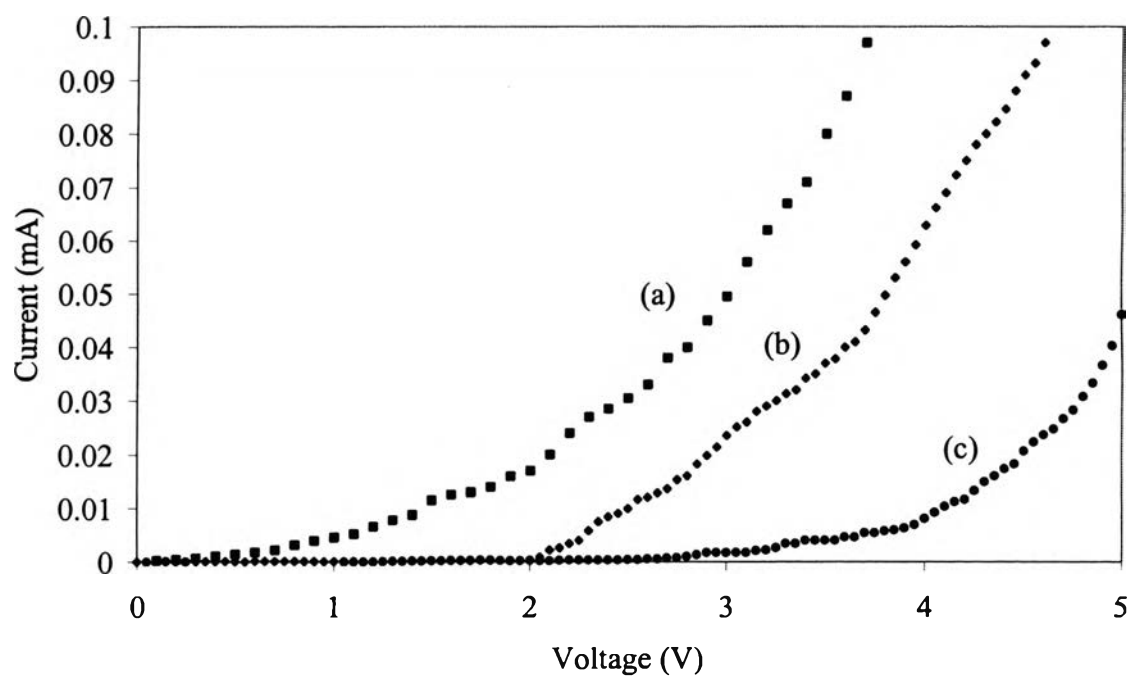


Figure 4.32 Relationship between current and voltage of LEDs based on (a) PPV, (b) PPV/OH-MMT 30 wt %, and (c) PPV/OH-MMT 60 wt %.

Moreover, Figure 4.33 and 4.34 show the turn-on voltage of PPV-clay nanocomposites and protein-clay nanocomposites, respectively. The turn-on voltage increased with OH-MMT content. However, the turn-on voltage tended to saturate with higher clay loading.

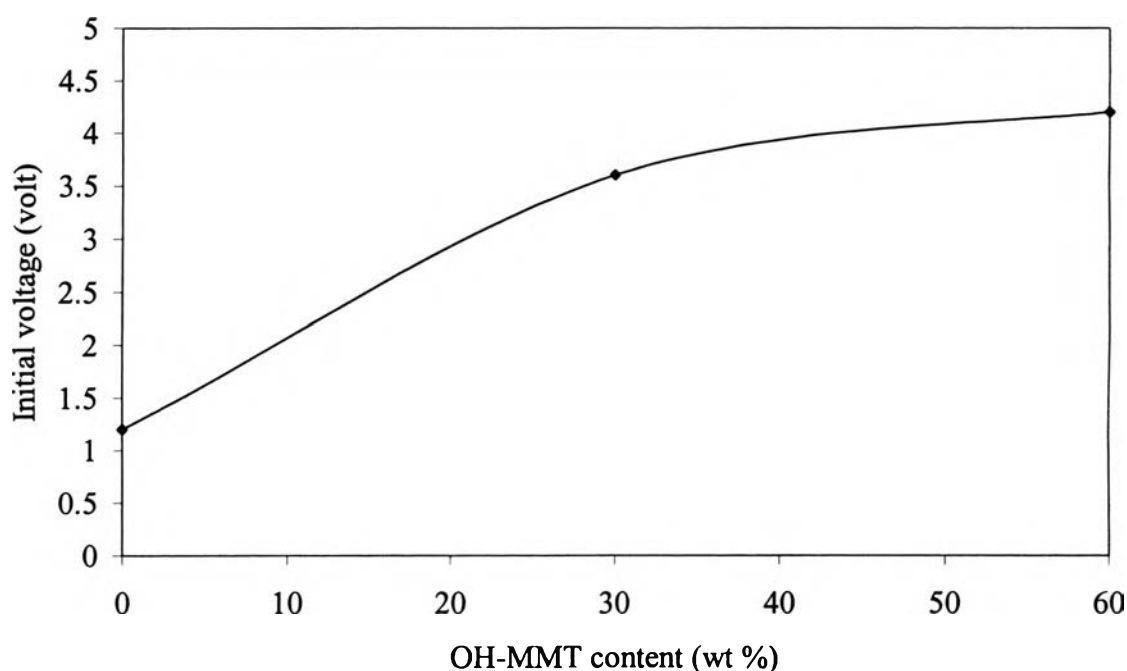


Figure 4.33 Effect of organophilic-clay on the turn-on voltage of LEDs based on PPV-clay nanocomposites.

The current in I-V curves tended to reduce with increasing organically modified clay content. Due to stacking layer of clay nanoparticles, the flow of electrons and holes were blocked and more electrical voltage was needed. This charge carrier blocking caused the recombination of bipolar to be more probable and lengthens the lifetime of the exciton formation. The explanation was confirmed by the results of time-resolved photoluminescence experiment which showed longer radiative lifetime with higher composition of modified montmorillonite.

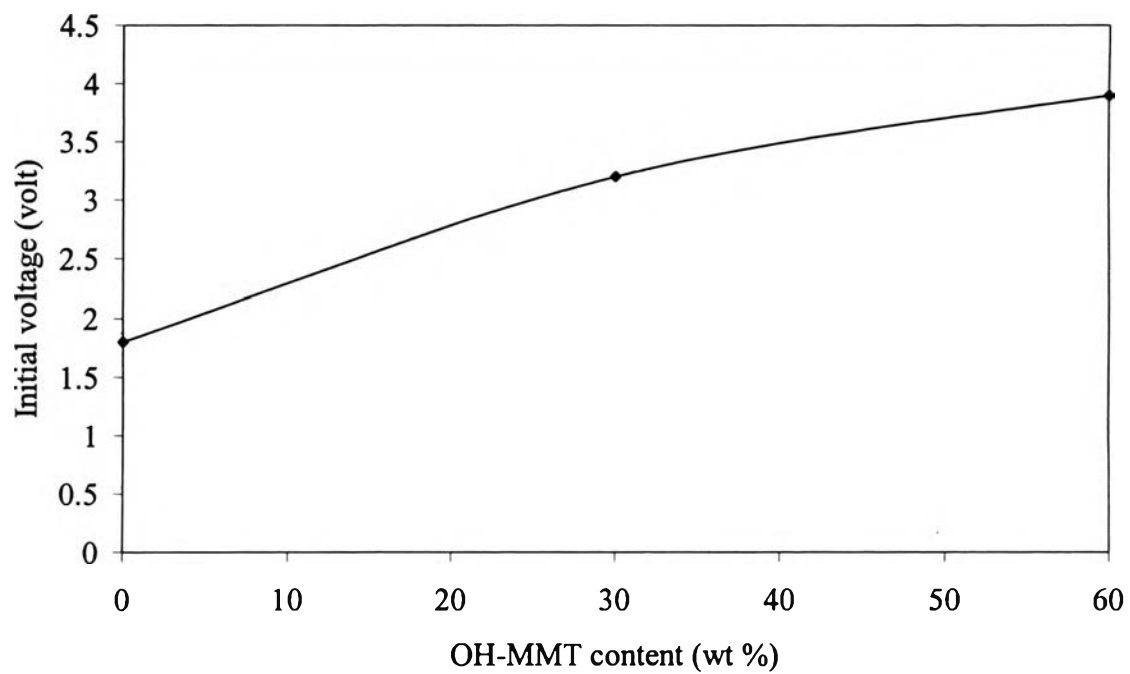


Figure 4.34 Effect of organophilic-clay on the turn-on voltage of LEDs based on protein-clay nanocomposites.